Skyrme energy functional and low lying 2^+ states in Sn, Cd, and Te isotopes

P. Fleischer, P. Klüpfel, and P.-G. Reinhard*
Institut für Theoretische Physik II, Universität Erlangen, D-91058 Erlangen, Germany

J. A. Maruhn
Institut für Theoretische Physik, Universität Frankfurt, D-60325 Frankfurt, Germany
(Received 29 October 2003; revised manuscript received 22 July 2004; published 29 November 2004)

We study the predictive power of Skyrme forces with respect to low lying quadrupole spectra along the chains of Sn, Cd, and Te isotopes. Excitation energies and $B(E2)$ values for the lowest quadrupole states are computed from a collective Schrödinger equation which is deduced through a collective path generated by constraint Skyrme-Hartree-Fock (SHF) plus self-consistent cranking for the dynamical response. We compare the results from four different Skyrme forces, all treated with two different pairing forces (volume versus density-dependent pairing). The region around the neutron shell closure $N=82$ is very sensitive to changes in the Skyrme while the midshell isotopes in the region $N<82$ depend mainly on the adjustment of pairing. The neutron rich isotopes are most sensitive and depend on both aspects.

DOI: 10.1103/PhysRevC.70.054321 PACS number(s): 21.10.Dr, 21.10.Pc, 21.60.Jz

I. INTRODUCTION

A key feature of nuclear excitations is the low-lying 2^+ states. Their properties delivered crucial input for developing an understanding of nuclear structure [1,2]. At first glance, they suggest the collective picture of the nucleus as a liquid drop which can undergo global quadrupole oscillations and which freeze under certain conditions to a stable rotator. This view has been formulated in terms of the Bohr-Hamiltonian, which establishes a collective dynamics in the five quadrupole degrees of freedom [3]. The parameters of the collective Hamiltonian have to be adjusted phenomenologically, see, e.g., the applications in [4]. The collective approach has been revived with the interacting boson model (IBM), which has found widespread application and was proven to be extremely useful in sorting nuclear low-energy spectra [5].

The collective picture is seemingly in contrast to the microscopic view, which sees the nucleus as consisting of shells of single nucleons arranging themselves in a common mean field [6,7]. The views can be unified by the concept of a deformed mean field, which establishes a relation between a single-particle shell structure and global deformations [8,9]. The collective motion is then understood as vibration (or rotation) of the mean field similar to the Born-Oppenheimer method for describing molecular vibrations. The connection is established on a formally sound level by the generator coordinate method (GCM) [10,11], which describes collective dynamics as coherent superposition of a continuous set of deformed mean-field states, called the collective path. The GCM within the Gaussian overlap approximation (GOA) allows us to establish contact between the microscopic foundation and a collective Bohr-Hamiltonian [12,13]. Starting from the GCM, the lines of applications spread enormously. There are, on the one hand, fully fledged GCM calculations which skip the collective Hamiltonian as an intermediate level and compute low-energy spectra directly from the coherent superposition of the collective path; these sophisticated calculations imply exact projection for the conserved quantities, as particle number, angular momentum, and center of mass; there are many published results around (we mention here [14,15] as two recent examples). On the other hand, one finds several approximations to the microscopic computation of the Bohr-Hamiltonian; most applications hitherto employ a phenomenological shell model to describe the deformed mean field, see, e.g., [16]. There are also several self-consistent calculations along that line; for an early example, see [17] and for more recent achievements see [18,19].

An alternative direction of development remains at the microscopic mean-field description and makes it manageable by restricting considerations to small-amplitude motion. This yields the much celebrated random-phase approximation (RPA), which has its stronghold in the description of giant resonances, see, e.g., [20]. The appropriate extension to nonclosed shells with pairing is the quasiparticle RPA (QRPA), which has only recently been developed up to a rigorously self-consistent level [21]. The QRPA describes formally the whole excitation spectrum, including the low lying 2^+ states, and it optimizes all states automatically. It assumes, however, small amplitudes, i.e., harmonic motion. This is perhaps legitimate close to magic nuclei but somewhat dubious elsewhere. The above mentioned theories for large-amplitude collective motion concentrate on the lowest state only but try to take into account all effects of anharmonicity due to soft potential energy landscapes and shape isomerism. The fully fledged adiabatic time-dependent Hartree-Fock method (ATDHF) provides an unambiguous optimization scheme for the large-amplitude collective path [12,22]. However, that rather involved scheme has not yet been used for heavy nuclei, as we are going to study here. We use presently ATDHF only to compute the self-consistent collective mass and employ the more intuitive constraint Hartree-Fock method to generate the path.

*Electronic address: reinhard@theorie2.physik.uni-erlangen.de

The connection from a microscopic Hamiltonian to collective spectra via a large-amplitude collective path is well established by virtue of the GCM. An open problem is the microscopic input. Self-consistent nuclear mean-field models employ effective energy functionals such as, e.g., the Skyrme-Hartree-Fock method, the Gogny force, or relativistic mean field; for a recent review, see [23]. These are empirically adjusted to nuclear ground-state properties of stable nuclei. There exists a large number of equivalent parametrizations which provide comparable ground-state properties but can differ substantially in predictions to exotic nuclei or resonance excitations [23,24]. It is by no means guaranteed that all mean-field parametrizations produce at once the correct collective low-energy vibrations. The contrary is to be expected, namely a broad span of predictions among which only a few parametrizations deliver a satisfying spectrum. To phrase that positively, low-energy vibrations provide useful information for a better selection of mean-field parametrizations. We aim here at a first exploration of the connection between mean-field parametrizations and emerging low-energy spectra. We do that for the Skyrme-Hartree-Fock approximation by comparing the results of several different Skyrme forces and pairing recipes.

It is obvious that such systematic studies need to confine the subject and the method in order to keep things manageable. As test cases, we consider the lowest 2^+ state in the chain of Sn isotopes and its even neighbors Cd and Te. These share basically one type of collective motion being predominantly soft vibrators. For the practical technique, we employ GCM-GOA through a microscopically computed Bohr-Hamiltonian. For reasons of simplicity, the microscopic information is computed along axially symmetric shapes and interpolated into the full space of quadrupole degrees of freedom. This approximation allows large-scale scans and it is acceptable for soft vibrators as they are studied here.

II. FORMAL FRAMEWORK

A. Underlying microscopic model: Input parameters

As a starting point, we take a microscopic mean-field theory at the level of the Skyrme-Hartree-Fock model augmented by pairing in the BCS approximation plus the Lipkin-Nogami correction for approximate particle number projection. This is a standard approach in nuclear structure physics. We refer the reader to [23] for a detailed description of the energy functional and subsequent mean-field equations. We recapitulate here only briefly the spectrum of variants of that model, which will play a major role in the following discussions.

The mean-field part is determined by the Skyrme energy functional $E_{\rm Sk}(\rho_\nu,\tau_\nu,\mathcal{J}_\nu,j_\nu,\sigma_\nu)$ which depends on the local density ρ_ν, kinetic-energy density τ_ν, spin-orbit density $\mathcal{J}_\nu$, current j_ν, and spin-density σ_ν, and where q means protons or neutrons. The functional form has been basically settled for two decades [25] with minor extensions in later stages (e.g., [26,27]). However, there exists a great variety of actual parametrizations for the Skyrme energy functional. Most of them provide a high-quality description of nuclear bulk properties as binding energies and radii. They differ in details as, e.g., isovector forces or surface properties. We are going to apply here the Skyrme functionals to a regime far from what had been considered in the fits. It is thus important to explore a minimal variation of parametrizations within the Skyrme framework. We will consider here SkM* as a widely used traditional standard [25], Sly6 as a recent fit which includes information on isotopic trends and neutron matter [28], SkI3 as a fit which maps the relativistic isovector structure of the spin-orbit force and takes care of the surface thickness [26], and SkO [29] as a recent fit relying on the same fit data as SkI3 but with additional constraint on the two-nucleon separation energies around ^{208}Pb and with a better adjusted asymmetry energy. That selection contains a large span of effective masses: SkI3$\leftrightarrow m^*/m=0.6$, SLy6$\leftrightarrow m^*/m=0.7$, SkM*$\leftrightarrow m^*/m=0.8$, and SkO$\leftrightarrow m^*/m=0.9$. The effective mass has an influence on the level density near the Fermi surface, which, in turn, may have an effect on the low-energy collective states. There is also a difference in the isovector and spin-orbit properties. Besides the effective mass and asymmetry, the bulk parameters (equilibrium energy and density, as well as incompressibility) are comparable.

TABLE I. Pairing strengths for the two pairing recipes and for the Skyrme forces used in this paper. The strengths are given in units of fm^{-3}.

	$V_p^{(\rm DI)}$	$V_n^{(\rm DI)}$	$V_p^{(\rm DDDI)}$	$V_n^{(\rm DDDI)}$
SkM*	279.1	259.0	990.0	802.0
SLy6	298.8	288.5	1053.1	864.2
SkI3	335.4	331.6	1233.0	996.0
SkO	253.0	269.0	1007.4	893.7

The second key ingredient is pairing. A present-day standard is to use a zero range pairing force often called volume pairing. We will use the notion δ-interaction (DI) pairing. A widely used variant for the pairing force is a density-dependent δ interaction (DDDI) [30]. Both recipes are summarized as

$$V^{(\rm pair)}=\begin{cases} V_\nu^{(\rm DI)}\delta(r_1-r_2) \\ V_\nu^{(\rm DDDI)}\delta(r_1-r_2)[1-\rho(\overline{r})/\rho_0]. \end{cases} \tag{1}$$

The pairing strengths or $V_\nu^{(\rm DDDI)}$ are adjusted to odd-even staggering of binding energies in a few representative semimagic nuclei (Sn and Pb isotopes, $N=82$ isotones). The adjustment is done for each force separately because the much different effective masses call for different pairing strengths. The actual values used here are given in Table I.

The pairing recipe is to be augmented by a cutoff in single-particle space. We use a smooth cutoff with a Woods-Saxon profile in the single-particle energies. The switching energy is chosen such that the pairing space covers $1.6N^{2/3}$ particles above the Fermi energy; for details, see [31]. In order to explore the influence of the pairing recipe, we will also discuss deliberate rescaling of the pairing strengths.

B. Deduced collective dynamics

The mapping from the microscopic to a collective description is performed with the generator-coordinate method

(GCM). This is a much celebrated method in nuclear structure physics; for a review see, e.g., [12] and for a brief summary see [23]. We outline here the basic steps and provide a more detailed compact account in Appendix I.

The stationary mean-field equations as such provide only a few well isolated states, preferably the ground state and perhaps some isomers. Each state is characterized by one BCS wave function $|\Phi\rangle$ which is composed of a set of single-nucleon wave functions together with their occupation amplitudes. In order to describe motion, one needs to consider a time-dependent mean-field theory, in the nuclear community often called time-dependent Hartree-Fock (TDHF). Large-amplitude collective motion is related to low-energy excitations, thus slow motion. This justifies the adiabatic limit known as ATDHF. It yields at the end a collective path $\{|\Phi_q\rangle\}$, where q stands for continuous series of deformations, predominantly of quadrupole type because nuclei are softest in that degree of freedom. The dynamical aspect is added in first order of collective velocity, i.e., in terms of linear response to a collective displacement. It is a widely used approximation to determine the collective path from quadrupole constrained Hartree-Fock-BCS (CHF).

A systematic theory for an optimized collective path is provided by adiabatic TDHF (ATDHF) [32–34]. The overwhelming majority of practical applications simplifies the construction by using a simple quadrupole constraint Hartree-Fock to produce the $|\Phi_q\rangle$. The path, once established, serves as a basis along which the collective motion expands. The corresponding microscopic state is described as a collective superposition $|\Psi\rangle = \int dq |\Phi_q\rangle f(q)$. The state $|\Psi\rangle$ is optimized by a variational principle. This is the fully fledged GCM, which can be attacked in a straightforward numerical manner, see, e.g., [14,15,35]. However, that is still a very demanding task and not so well suited for broad surveys as we intend it here. As a simple, efficient, and reliable shortcut, we use here the Gaussian overlap approximation (GOA), which parametrizes the norm and Hamiltonian overlap in terms of Gaussians, e.g., for the norm overlap as $\langle\Phi_q|\Phi_{q'}\rangle = \exp[-\lambda(q-q')^2/4]$. It provides an acceptable approximation, particularly for medium and heavy nuclei [12,36]. The GCM-GOA yields at the end a fairly simple collective Hamiltonian where the collective potentials and masses are unambiguously computed from the microscopic energy functional and the collective path. Quadrupole motion has five degrees of freedom [3–5]. The emerging collective Hamiltonian thus has the form of a generalized Bohr-Hamiltonian while its potentials and masses are computed from microscopic input [16,18,19].

The practice of GCM-GOA is a bit involved; see the Appendix for a few more details. We summarize here the steps. The energy expectation value along the path yields a raw collective potential $\mathcal{V}(q)$. The collective mass and moments of inertia are obtained by dynamical linear response about a given point at the path often called self-consistent (or ATDHF) cranking [33]; as an approximation, Inglis cranking is used whenever justified. Zero-point energy corrections to the potential are computed from these masses and the collective fluctuations (quadrupole, angular momentum) of the states $|\Phi_q\rangle$. In fact, a topologically corrected GOA is used to allow a numerical robust computation of potentials and masses in the intrinsic frame (defined by a diagonal inertia tensor) [36,37]. This provides an interpolation scheme to connect safely the near-spherical shapes with larger deformations.

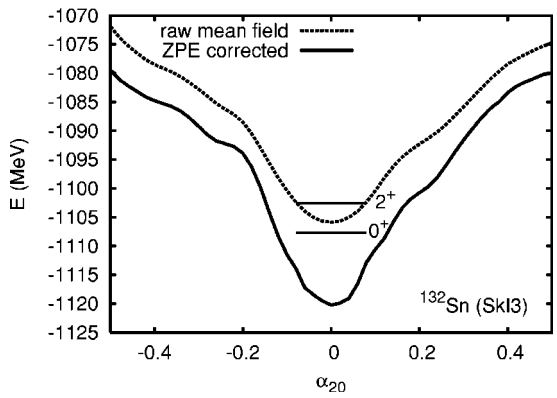

FIG. 1. The raw collective potential $\mathcal{V}$ and the effective potential V including the zero-point energy corrections (A6), both drawn as function of the intrinsic axial quadrupole momentum a_{20}. Test case is ^{132}Sn computed with DI pairing and SkI3. The position of the 0_0^+ ground state and the first 2^+ state are indicated by horizontal bars. The difference between the minimum of $\mathcal{V}$ and the 0_0^+ energy is the correlation energy $\Delta E_{\rm corr}$.

After all, we restrict the microscopic calculations to axial symmetry. The fully five-dimensional quadrupole dynamics is recovered by interpolation of the collective potential and masses between prolate and oblate shapes into the triaxial plane. This approximation saves two orders of magnitude computation time and thus allows the large-scale systematics as we intend it here. On the other hand, it is well justified at and in the vicinity of the spherical shape. The test cases for the present study are Sn isotopes and its even-even neighbors Cd and Te, which are predominantly soft vibrators around spherical mean. Moreover, we confine the study to the first excited 2^+ state (and occasionally to the 0^+ ground state) which both are not very sensitive to details in the triaxial plane. All that considered, the triaxial interpolation is a useful and legitimate approximation for the intended systematic explorations.

C. An example for potentials and masses

In order to exemplify details of the calculations, Fig. 1 shows for the case of ^{132}Sn the collective potential before and after zero-point energy correction (ZPE) (A6). The ZPE induce obviously a strong global down-shift in energy because the spurious energy content from collective fluctuations in the $|\Phi_q\rangle$ is subtracted. Moreover, they may change the shape of the potential. The corrected potential has its minimum at a slightly deformed position, although the doubly magic ^{132}Sn is a perfectly spherical nucleus in a pure mean-field description (see the well defined spherical minimum in $\mathcal{V}$). This is the same effect as happens in variation after rotational projection (for a model discussion, see [36]): knowing that the projection restores spherical shape anyway, the system takes advantage of a small deformation to acquire correlation energy. It is comforting that we see the same

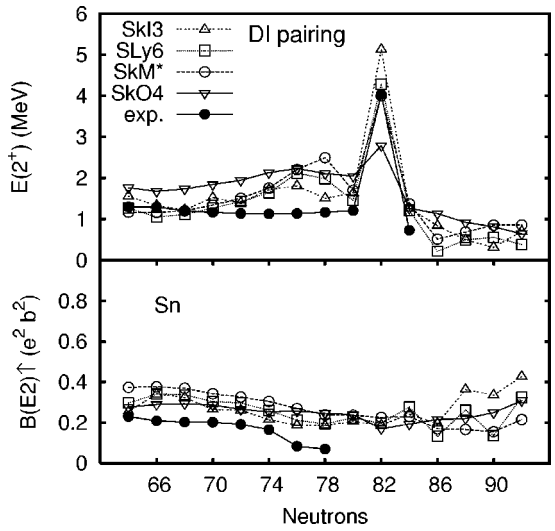

FIG. 2. Energies $E(2^+)$ and $B(E2)\uparrow$ values $(=|\langle 0^+|Q_{2M}|2^+\rangle|^2)$ along the chain of Sn isotopes calculated using the four different Skyrme interactions as indicated. The experimental results are taken from [38].

effect here because our treatment of quantum correction should include a good approximation to rotational projection.

Figure 1 also indicates the position of the 0_0^+ ground state and the first excited 2^+ state. The 0_0^+ lies above the bottom of the intrinsic potential V as it should be, to account for the correct physical zero-point energies, but it stays below the minimum of the raw potential $\mathcal{V}$ because the larger spurious zero-point energy had been subtracted before adding the physical one. The net effect is a correlation energy $\Delta E_{\rm corr}$ which expresses that the collectively correlated ground state is better bound than the mean-field ground state. The 2^+ state lies, of course, above the 0_0^+ state. The quantity of interest here is the excitation energy $E(2^+)$, which is computed as the difference between the total 2^+ energy and the 0_0^+ energy.

III. RESULTS

A. Results for the chain of Sn isotopes

1. Variation of forces

Figure 2 shows the 2^+ excitation energies and transition strengths along the chain of Sn isotopes for the four chosen SHF parametrizations and in comparison to experimental data. At first glance, we see that all calculations hit the right order of magnitude. They also reproduce the increase of the E_{2^+} at the shell closure $N=82$. At closer inspection, however, we see interesting differences and mismatches in detail.

Let us first concentrate on the doubly magic case of $N=82$. Shell effects directly related to the SHF forces should dominate here. And indeed, we see that the $E(2^+)$ are closely related to spectral properties. Table II shows the $E(2^+)$ energies in comparison to the spectral gaps of protons and neutrons in ^{132}Sn. The spectral gaps are the energy difference between the highest occupied single-particle orbital and the lowest unoccupied orbital (known as HOMO-LUMO gap in molecular physics). The neutrons show always the smaller

TABLE II. Comparison of the $E(2^+)$ energies in ^{132}Sn for the various Skyrme forces with the spectral gaps in ^{132}Sn and the effective mass m^*/m associated with the forces.

Force	SkI3	SLy6	SkM*	SkO
$E(2^+)$ (MeV)	4.36	3.76	3.94	2.41
spectral gap protons (MeV)	6.6	6.2	6.4	6.0
spectral gap neutrons (MeV)	6.6	6.0	5.4	4.0
m^*/m	0.6	0.7	0.8	0.9

gaps and these lowest one-particle–one-hole $(1ph)$ transitions take the lead in the composition of the lowest 2^+ state. Correspondingly, both quantities share the same trends. The spectral gap, in turn, is related to the effective mass m^*/m of the forces. We see that also in Table II where low m^*/m correlate to large gaps and vice versa. But the step down to the rather low spectral gap for SkO is much larger than the step up in effective mass. Here we see also an interference from the very strong isovector spin-orbit force of SkO, another important contributor to shell effects. Table II furthermore, demonstrates the effect of the residual interaction in that the $E(2^+)$ are generally 1.5 MeV below the lowest $1ph$ energy. This allows us to postulate a simple criterion for the selection of forces: the lowest spectral gap in ^{132}Sn (and other doubly magic nuclei) should stay safely above the experimental $E(2^+)$, which is 4.04 MeV for ^{132}Sn. The force SkO clearly fails in that respect. The reason is that SkO was fitted to match the two-nucleon shell gaps at doubly magic ^{208}Pb already at the level of pure mean-field calculations [29]. Meanwhile, it has been shown that collective correlations reduce the two-nucleon shell gaps by 1–2 MeV [39]. The fitting strategy of SkO thus squeezes the spectral gap too much with the obvious consequence that the collective spectra are spoiled throughout. This mismatch is thus a strong hint on the inner coherence of Skyrme forces connecting the various observables.

Far away from the magic $N=82$, one expects that the pairing gap dominates the $E(2^+)$ energy. The pairing force was tuned in the same way to the odd-even staggering in Sn isotopes and $N=82$ isotones. Thus the pairing gap is about the same for all four Skyrme forces in the well pairing region $(N<80)$. We see indeed comparable energies for the three forces, SkM*, SLy6, and SkI3, which also hit very nicely the experimental values. The force SkO, however, produces systematically larger energies out there. This shows that shell effects (here probably from the spin-orbit force) have also some influence. Different relations are seen in the other pairing regime for the neutron rich, exotic nuclei above $N=82$ where SkM* shows always the largest energies. This is at the same time a region of weak binding. This causes a strong interplay of shell effects and pairing which are not easily disentangled.

Large differences are seen in the immediate vicinity of $N=82$. All forces, expect SkO, reproduce nicely the sudden step down from $N=82$ and the asymmetry around $N=82$, namely the fact that $N=84$ has lower $E(2^+)$ than $N=80$. But the results differ in the trends for $N=78$. The case SkI3 follows nicely the smooth experimental trend while SkM* and

SLy6 show a spike. That is compensated at $N=70$ where now SkI3 has a spike. In all these cases, we found that a larger $E(2^+)$ is related to a somewhat lower neutron level density at the Fermi surface.

A much more critical test than excitation energies are the associated transition probabilities, the $B(E2)$ values. One is usually happy to describe them within a factor of 2 or so, and often the concept of effective charges is introduced to achieve a fine-tuning [40]. The lower panel of Fig. 2 shows the $B(E2)\uparrow$ values for the transitions. For $N\leqslant 82$, they are similar for all four forces in spite of the sometimes very different energies. But they all differ from the experimental data by about a factor of 2. The positive aspect is that the theoretical results come so close at all in view of the fact that the transition strengths are always much more demanding. The remaining mismatch can have various origins: (1) We use simply a quadrupole constraint to generate the collective path instead of the variationally optimized ATDHF prescription [32–34]. (2) We use the raw quadrupole expectation value rather than the fully mapped collective image (see Appendix A6). (3) The effective energy functional is not fully suited to compute transition moments and effective charges had to be added for a correct description [40]. Which one of these approximations is most responsible has yet to be explored. Anyway, the results are not untypically bad because almost all microscopic approaches have a hard time with an exact reproduction of transition moments.

The $B(E2)\uparrow$ in the region around the doubly magic ^{132}Sn surprisingly shows basically no differences between the forces, just in a region where the energies differ most. A very interesting point is the magic ^{132}Sn. Naive models predict a dramatic drop in the $B(E2)$ at the magic point. A model study taking care of the residual interaction and cross-talk between the neutron and proton quadrupole vibrations predicts that the $B(E2)$ should, quite oppositely, have a peak at ^{132}Sn [41]. Our calculations confirm these estimates at a qualitative level, namely to the extent that we also do not find any deep dip in the $B(E2)$. In our cases, the residual interaction was obviously not large enough to turn that into a peak. But these are quantitative details of the employed forces.

The largest differences between forces for the $B(E2)\uparrow$ values are seen in the deep exotic regime $A>132$. We are sure that information about $B(E2)$ in that region would be valuable. But before one can exploit that, one has to understand (and possibly remove) the systematic overestimation still seen on the low-A side.

2. Variation of pairing recipes

Figure 3 shows the collective spectra along the Sn chain for SkI3 computed with different pairing prescriptions. We have added in the lowest panel some information about the internal pairing structure, namely the average neutron-pairing gaps $\bar{\Delta}=\Sigma_\alpha u_\alpha v_\alpha \Delta_{\alpha\alpha}/\Sigma_\alpha u_\alpha v_\alpha$ which are deduced from spectral properties of the given nucleus at the spherical shape (usually the minimum in the PES) and which, nonetheless, provide a simple measure for the pairing gap deduced from odd-even staggering [31]. The deliberately changed pairing strengths (boxes versus circles for enhanced pairing and rhombus versus circle for reduced pairing) have an obvious effect. The pairing gap is increased or reduced and, subsequently, the $E(2^+)$ energies change in the same direction. The effect is most pronounced in the regions sufficiently far off $N=82$, where we expect a dominance of pairing in the collective spectra. The relative changes in excitation energies and pairing gaps are much larger than the change in pairing strength. Moreover, the excitation energies behave generally similar to the pairing gaps. This demonstrates that the low-energy spectra in soft vibrators provide valuable information about the pairing strengths. One is tempted to use that for an immediate tuning of the strengths. We run, however, into some conflict, because $E(2^+)$ energies and $B(E2)\uparrow$ do not coincide at the same strength. Moreover, one has to keep in mind that the information from lying states is still mixed with effects of the mean field. This is a general feature of nuclear structure, even for the odd-even staggering, which is usually taken as a benchmark for pairing properties [42]. The interference of shell effects can be seen here particularly well from some irregularity at $N=68$. The reduced pairing produces for $N=68$ a strongly deformed ground state which results in a sudden drop of the $E(2^+)$ energy accompanied by a strong peak in $B(E2)\uparrow$. The average gap shows no dramatic reaction because it remains related to the now irrelevant spherical shape. The DDDI pairing stays in most cases more or less close to the results of DI pairing, which is somewhat expected because it is tuned to

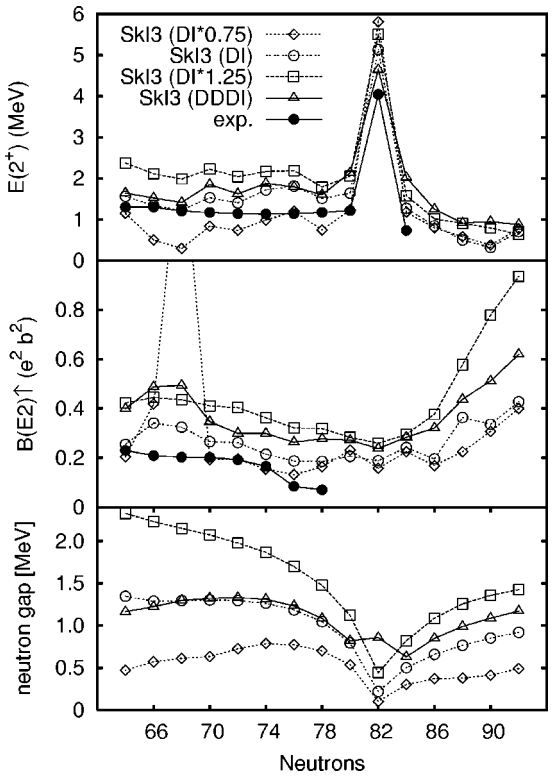

FIG. 3. Energies $E(2^+)$, $B(E2)\uparrow$ values ($=|\langle 0^+|Q_{2M}|2^+\rangle|^2$), and average neutron-pairing gaps at spherical shape along the chain of Sn isotopes calculated with SkI3 and three different pairing recipes: standard DI (circles), DDDI (boxes), and DI with 25% enhanced strength. The experimental results are taken from [38].

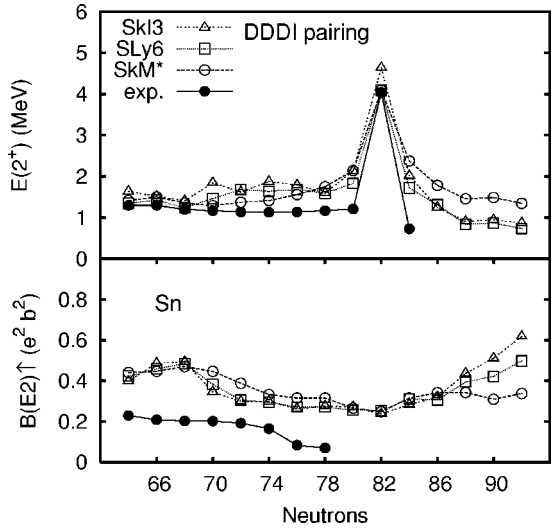

FIG. 4. As Fig. 2, but now with DDDI pairing.

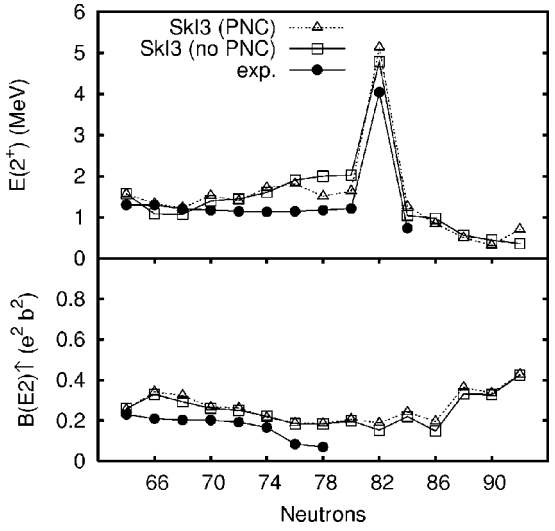

FIG. 5. Energies $E(2^+)$ and $B(E2)\uparrow$ values ($=|\langle 0^+|Q_{2M}|2^+\rangle|^2$) along the chain of Sn isotopes computed with SkI3 and DI pairing, once with (solid line, full circles) and once without (dashed line, open circle) particle number restoration as outlined in Appendix (A4). The experimental results (dotted lines, full squares) are taken from [38].

the same average pairing gap. However, DDDI pairing reacts differently to shell effects, as can be seen in the vicinity of the shell closure $N=82$ and for the weak shell closure which SkI3 produces at $N=72$. The DI pairing seems to comply better with data. But that holds in connection with the particular shell structure of SkI3. Much more systematic investigations with varied forces and in other region of the nuclear chart are necessary before drawing any conclusion like that. The $B(E2)\uparrow$ values shown in the lower panel of Fig. 3 show generally smooth trends, except for $N\geqslant 86$, where an increasing trend sets on which is related to the increasing softness of these neutron-rich isotopes. The sensitivity to varying pairing recipes is similar to what we have seen when varying the forces: They vary little for $N\leqslant 82$ and more significant differences appear in the far exotic regime $N>82$.

For completeness, it is worthwhile to look at the performance of DDDI pairing also for the other Skyrme forces in the survey. That is shown in Fig. 4. It has to be compared with Fig. 2. Similarities and differences are about the same for all shown forces. The average excitations in the well pairing regime are comparable. The small fluctuations about the average trends appear for DDDI at different places than for DI pairing. The most pronounced difference to DI is seen for the $E(2^+)$ energy next to the magic neutron number, i.e., for $N=80$ and 84. DI pairing reproduces the steep experimental drop while the DDDI results make a somewhat less dramatic step. The $B(E2)\uparrow$ values shown in the lower panel are very similar to those from DI pairing. They seem here to be the more robust signal. We conclude from these results that the $B(E2)\uparrow$ are insensitive to pairing while they are the much more sensitive observable in other respects, e.g., in its dependence on the force.

A final comment on the $B(E2)\uparrow$ values: Good vibrators and well-developed rotators are distinguished by the fact that the lowest 2^+ state exhausts the quadrupole sum rule in collective space. The test for this feature is the comparison of the variance (= quadrupole sum rule) with the $B(E2)$ value,

$$\langle 0^+|Q_{20}^2|0^+\rangle = \sum_n |\langle 2_n^+|Q_{20}|0^+\rangle|^2 \stackrel{?}{=} |\langle 2_1^+|Q_{20}|0^+\rangle|^2, \qquad (2)$$

where $\langle\cdots\rangle$ means the average in collective space, 0^+ the ground state, 2_n^+ the spectrum of 2^+ states, and 2_1^+ the lowest 2^+ state. We have checked that and found that there is generally good exhaustion of the variance by the lowest 2^+. The collective potential $\mathcal{V}(\alpha_{20})$ of all these isotopes excludes rotors, so that we can conclude that they are good vibrators.

3. Effect of particle-number correction

The collective Schrödinger equation contains the particle-number correction with $\hat{N}_{\rm coll}$ as discussed in Appendix A4. It is interesting to check the impact on collective properties.

This is done in Fig. 5. There is minimal difference for the $B(E2)\uparrow$ values. The main effect is seen for energies in the region of weak pairing, i.e., at and around shell closure. In fact, the particle-number corrected treatment seems to be a bit more sensitive to shell structure, as can be seen from the fact that calculations without the correction show generally smoother trends. But this statement should be taken with a grain of salt. The differences are anyway not very dramatic in view of the effects we see when comparing forces and pairing recipes.

B. Results for the isotopes of Cd and Te

The Sn isotopes have a magic proton number $Z=50$. It is interesting to have a look at its even neighbors, Cd with $Z=48$ and Te with $Z=52$. As a first impression, we show in Fig. 6 a direct comparison for a few selected isotones. The effect is obvious. The step from the magic proton number to the nonmagic ones reduces once more the $E(2^+)$ energies by

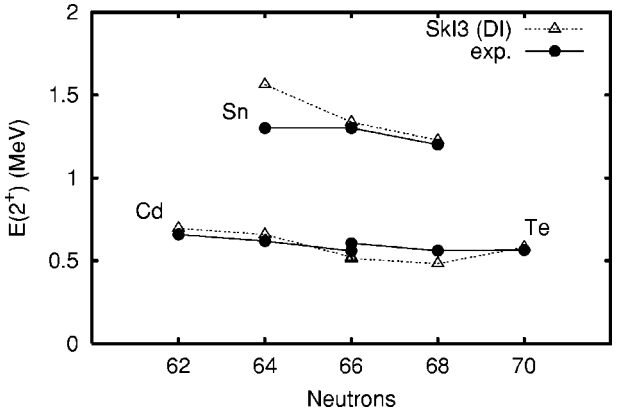

FIG. 6. Systematics of the energies of the first excited 2^+ states calculated with the microscopic Bohr-Hamiltonian (A9) using the interaction SkI3 for the nearest even-even neighbors of ^{116}Sn. The experimental results are taken from [38].

a substantial factor, fully in agreement with the experimental findings. The quadrupole mode in Cd and Te is much softer than in Sn where the magic proton number enhances the rigidity of the whole mode due to a strong residual proton-neutron force [43].

A summary of results for the Cd and Te isotopes using the four different Skyrme interactions SkI3, SLy6, SkM*, and SkO is displayed in Fig. 7. For Te, the $E(2^+)$ from different forces are very close to each other and to the experimental data up to $N=76$ and show again larger differences near the shell closure $N=82$. The case for Cd is similar, showing, however, an earlier onset of differences. It is noteworthy that the results for SkO reside well among the other forces, although it behaved dramatically different for the Sn isotopes. This is related to the fact that shell effects are somewhat suppressed in Cd and Te because these have a nonmagic proton number. Figure 7 shows also as complementing information the $B(E2)$ values for the Cd and Te isotopes. The differences between the theoretical and the experimental values are for Cd in the same order of magnitude as in the case for the Sn chain. They tend to be much less for the Te isotopes for $N\leqslant 78$ where deviations stay below 20%. This looks like a remarkable agreement. But both agreement for Te and disagreement for Cd and Sn have yet to be understood in detail.

We have seen in the Sn chain that the step from DI to DDDI pairing makes the most differences next to the neutron shell closure. One has to suspect that a similar feature appears next to the proton shell closure. The Sn chain resides at $N=50$, which is a closed proton shell. Thus the neighbor chains for Cd and Te are in the most sensitive regime and we expect visible differences. The results on the low-lying 2^+ states along Cd and Te are shown in Fig. 8. We see indeed that the $E(2^+)$ energies are larger with DDDI, particularly near the neutron shell closure at $N=82$. The differences become again negligible far out in the well pairing regime. And, as for Sn, the $B(E2)$ values are totally insensitive. It is also clear that the DI results, here and in the Sn chain, are closer to the data. The same effect was already seen for the neutron channel in Fig. 3. The step of the $E(2^+)$ when moving away from a magic number is softer for DDDI than for DI. This produces somewhat too high $E(2^+)$ for $N=80$ and 84 in Fig. 3 and here for $Z=48$ and 52 in Fig. 7 versus Fig. 8. We just mention this observation. It is too early to draw far-reaching conclusions on the validity of DI versus DDDI. The difference is seen in the worst case, namely a nucleus in the weak pairing regime where we are not yet sure that the present pairing treatment (BCS plus Lipkin-Nogami) is fully appropriate.

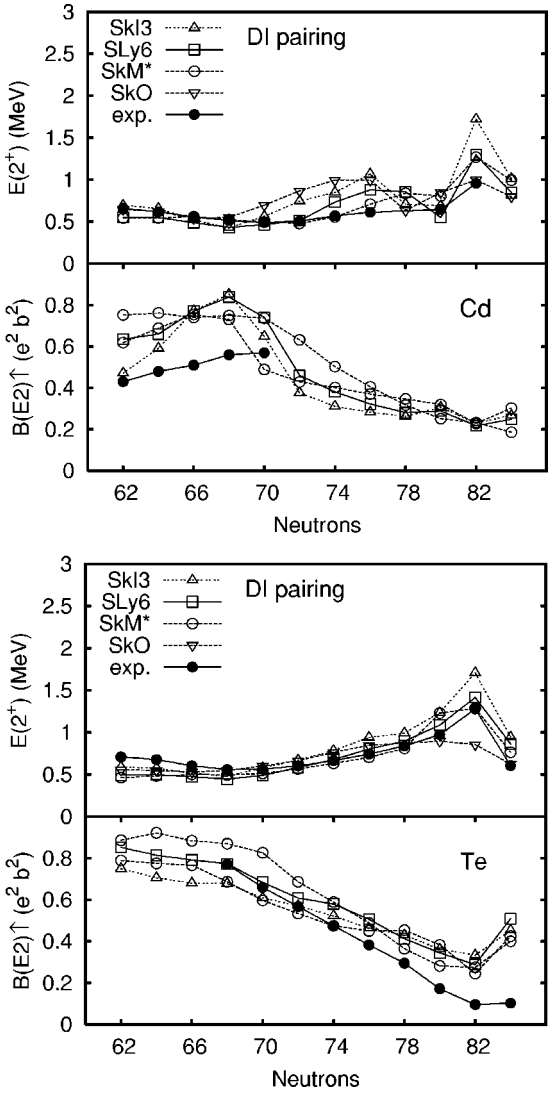

FIG. 7. Energies $E(2^+)$ and $B(E2)\uparrow$ values $(=|\langle 0^+|Q_{2M}|2^+\rangle|^2)$ along the chain of Cd isotopes (upper panels) and Te isotopes (lower panels) calculated with different Skyrme forces as indicated. The experimental results are taken from [38].

C. The isotope shifts for the Sn isotopes

The ground-state solution of the collective Schrödinger equation provides the collective ground-state correlations. One can compute the correlation effect on any one-body observable with the help of the collective map as outlined in Appendix A 6.

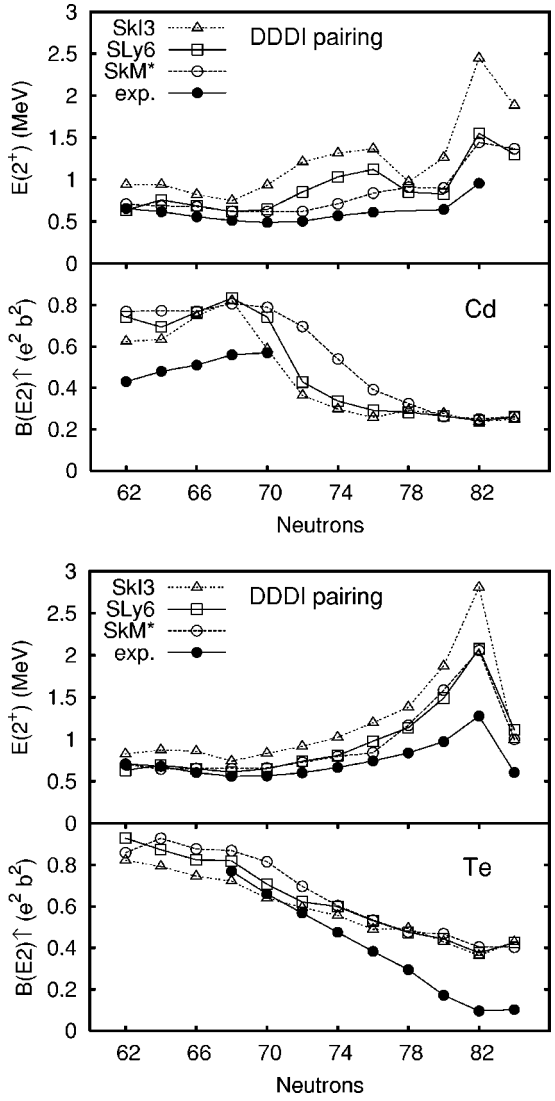

FIG. 8. As Fig. 7, but now for DDDI pairing.

Figure 9 shows results for the systematics of charge rms radii drawn in terms of isotope shifts relative to ^{116}Sn. The rms radii shown in the upper panel here are taken from the correlated ground state, which includes the collective shape fluctuations. At first glance, all forces reproduce the experimental trend very well where data are available. There remain small but significant differences between the four forces in that range among which SkI3 comes generally closest to the data. The similarity of the trends persists to isotopes with larger neutron numbers. Substantial differences develop at the upper end for the shown chain, i.e., for $N>86$. Not surprisingly, this is the regime of exotic nuclei because the generally soft binding amplifies small differences in shell structure. It is surprising, however, that these differences develop so late. The regime of similarity reaches well beyond the $N=82$ shell closure. This is due to the smoothing features of the shape fluctuations. The lower panel demonstrates the effect of ground-state correlations for that observable. There are practically no visible effects as compared to pure mean-field calculations, as one could have expected for such a chain of semimagic nuclei [26]. Correlation effects become

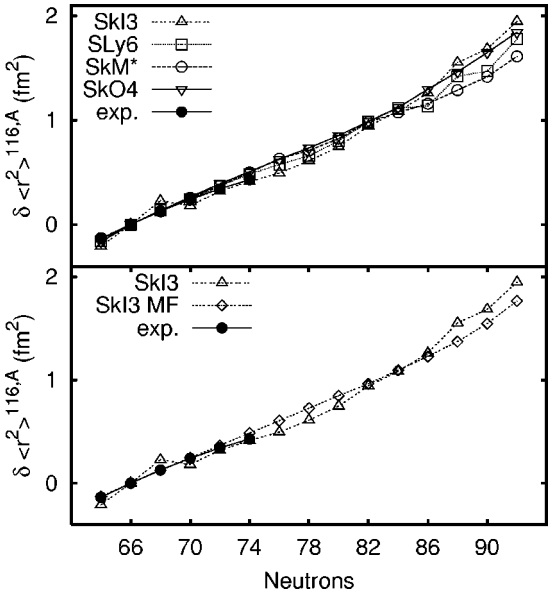

FIG. 9. Isotope shifts of the charge r.m.s radii, $\delta\langle r^2_{\rm rms}\rangle^{66,N}$, relative to ^{116}Sn. Upper panel: comparison of results from the four forces SkI3, SLy6, SkM*, and SkO including collective ground-state correlations. The expectation value $\langle r^2\rangle$ is calculated here according to Appendix (A6). Lower panel: Comparison of pure mean field result with those including correlations for the force SkI3. The experimental data are taken from [44].

visible again at the upper edge of the chain where the general softness of the deeply exotic nuclei also allows for larger shape fluctuations.

IV. CONCLUSION

We have investigated the predictive power of nuclear effective forces for describing low-lying collective states considering as test cases the chain of Sn isotopes as well as its even neighbors Cd and Te. As a particular example of such an effective force, we used the Skyrme-Hartree-Fock scheme augmented by a short-range pairing force. To that end, we used a representative sample of different Skyrme forces as well as two different pairing models (volume pairing versus density-dependent pairing). The spectra of collective quadrupole vibrations were computed in a two-step procedure: First, mean-field calculations with quadrupole constraint and self-consistent cranking were performed which provide the microscopic input for a collective Hamiltonian in terms of potentials, masses, and moments of inertia. Second, the collective Schrödinger equation thus obtained is solved in the space of the five quadrupole coordinates. Care has been taken to subtract correctly the zero-point energies from spurious collective fluctuations in the mean-field states and to respect the topology of the quadrupole space. As a simplification, we use axially symmetric mean-field calculations and interpolate triaxial properties between prolate and oblate shapes. This is an acceptable approximation for the nearly spherical soft vibrators considered in the present survey. Pairing is treated at the level of BCS with particle number correction in terms of the Lipkin-Nogami approximation. A

final fine-tuning of the average particle number is performed also for the collective states.

We find three regimes: collective properties are dominated by the pairing gap for $N \leqslant 76$, they are dominated by the spectral gap of the neutron level for $76 \leqslant N \leqslant 82$, and a sudden transition to prolate ground-state deformations emerges for $N > 82$. In the pairing dominated regime, the results for the 2^+ excitation energies depend mostly on the pairing strength and only weakly on the Skyrme forces (with the exception of the force SkO, which behaves a bit strange as a consequence of the constraint on the two-nucleon shell gas in the fit). As all pairing models used here were fitted to the odd-even staggering in the Sn region, we find generally nice agreement with experimental data in that midshell region. In the shell-gap-dominated regime, on the other hand, a strong sensitivity to the Skyrme force develops due to a strong relation to the spectral gap which, in turn, depends sensitively on the effective mass. These features persist into the regime above $N=82$. The result for the transition probabilities [the $B(E2)$ values] shows larger deviations from the data (up to a factor of 2). This is not surprising because $B(E2)$ values are generally more demanding to any model.

To summarize, we have shown that Skyrme forces have, in principle, the capability to describe low-lying collective spectra. In practice, the success depends on the actual parametrization used. Turning the argument around, we find that a systematic investigation of collective spectra delivers extremely useful information for the selection of parametrizations and the development of improved effective forces. This calls for more systematic investigations.

ACKNOWLEDGMENTS

We thank M. Bender, T. Bürvenich, and T. Cornelius for many clarifying and inspiring discussions. This work was supported in part by the Bundesministerium für Bildung und Forschung (BMBF), Project Nos. 06 ER 808 and 06 ER 124.

APPENDIX A: MICROSCOPIC COMPUTATION OF COLLECTIVE OPERATORS

1. The deformed mean field

The microscopic basis is a self-consistent mean-field according to SHF with DI or DDDI pairing (for details, see [23]). The SHF-BCS equations describe the nuclear state in terms of a set of single-particle states φ_n with associated BCS occupation amplitudes v_n. These together compose the BCS state $|\Phi\rangle = \Pi_n (u_n + v_n \hat{a}_n^+ \hat{a}_{-n}^+)|\text{vac}\rangle$ where $u_n = \sqrt{1-v_n^2}$. As a synonym for its content, we denote it by $|\Phi\rangle \equiv \{\varphi_n, v_n\}$. In practice, we go somewhat beyond the BCS scheme by using the Lipkin-Nogami (LN) approximation for particle number projection [45]. The mean-field equations can be summarized as

$$\left(\hat{h} - \sum_\nu (\epsilon_{\mathrm{F},\nu}\hat{N}_\nu - \epsilon_{2,\nu}\hat{N}_\nu^2) - \lambda \hat{Q}_{20}\right)|\Phi_{\alpha_{20}}\rangle = \mathcal{E}|\Phi_{\alpha_{20}}\rangle, \tag{A1a}$$

$$\hat{Q}_{20} = r^2 Y_{20} f_{\mathrm{cut}}(\mathbf{r}), \tag{A1b}$$

$$\alpha_{2m} = \frac{4\pi}{5}\frac{\langle \Phi_{\alpha_{20}}|r^2 Y_{2m}|\Phi_{\alpha_{20}}\rangle}{Ar^2}. \tag{A1c}$$

The $\hat{h}$ is a two-quasiparticle operator which itself depends on the state on which it acts. The actual form is obtained by a functional derivative of the given energy functional. The $\hat{N}_\nu$ is the operator of proton or neutron number. The Fermi energy $\epsilon_{\mathrm{F},\nu}$ is chosen to tune the correct particle number in the average, i.e.,

$$\epsilon_{\mathrm{F},\nu} \leftrightarrow \langle \Phi|\hat{N}_\nu|\Phi\rangle = N_\nu. \tag{A1d}$$

For simplicity, we write in the following one particle-number term as representative of both. The term $\propto \hat{N}_\nu^2$ accounts for the approximate particle-number projection and its parameter $\epsilon_{2,\nu}$ is given according to the LN recipe, taking properly into account the feedback from the mean field to the variances [45]. The LN scheme performs also an approximate variation after projection. This yields a finite pairing gap under any conditions, even at shell closures. And this is the feature we need to have a smooth evolution of the gap along the collective deformation path. Pure BCS can lead to discontinuities, which lead to discontinuities in the collective Hamiltonian.

The stationary mean-field equations without constraint provide only a few well isolated states, the ground state, and perhaps some isomers. In order to describe motion, one needs to consider a time-dependent mean-field theory, such as, e.g., time-dependent Hartree-Fock (TDHF). Large-amplitude collective motion is related to low-energy excitations, thus slow motion. This justifies the adiabatic limit known as adiabatic TDHF (ATDHF) [32,33]. It yields at the end an optimized constraint $\hat{Q}$ and subsequent collective path $\{|\Phi_q\rangle\}$, where q stands for a continuous series of deformations. The fully self-consistent optimization of the path is very cumbersome. It is a widely used approximation to use a simple quadrupole constraint as in Eq. (A1b). The anomalies at large distance are avoided by a cutoff function f_{cut} for which we use a Woods-Saxon shape [46]. The states are labeled with the dimensionless quadrupole moment (A1c), which is rescaled with the total particle number A and the rms radius r. The index m can run over -2, -1, 0, 1, and 2. The path will be computed only along axially symmetric shapes corresponding to $m=0$.

The numerical solution is done by standard methods. Wave functions and fields are represented on an axially symmetric grid in coordinate space. An accelerated gradient method is used to iterate the single-particle states φ_n into their stable solution [47] while the BCS+LN equations for v_n are solved in each iteration step. An extra iterative loop is included to maintain a wanted value of α_{20} [48].

Knowing the path yields immediately the raw collective potential as

$$\mathcal{V}(\alpha_{20}) = E_{\mathrm{SHF}}(|\Phi_{\alpha_{20}}\rangle), \tag{A2}$$

where E_{SHF} is the total SHF+BCS+LN energy for the given mean-field state $|\Phi_{\alpha_{20}}\rangle$ including a c.m. correction as appro-

priate for the given force [23]. The actual computations exploit explicit expressions in terms of the single-particle states φ_n and their occupation amplitudes v_n.

2. Computation of masses

The collective path allows us to define a collective momentum operator as the generator of deformation $\hat{P}_\alpha|\Phi_{\alpha_{20}}\rangle = i\partial_{\alpha_{20}}|\Phi_{\alpha_{20}}\rangle$. At the same time, $\hat{P}_\alpha$ can also be interpreted as the momentum operator associated with collective dynamics. The collective path $\{|\Phi_{\alpha_{20}}\rangle\}$ is complemented by the dynamical response of the system by adding a dynamical constraint $-\mu\hat{P}_\alpha$ to the mean-field equations, yielding eventually a dynamical collective path. The adiabatic approximation allows us to handle the dynamical part in the linear regime, i.e.,

$$|\Phi_{\alpha_{20}p_\alpha}\rangle \approx (1 + ip_\alpha\hat{Q}_\alpha^{(\mathrm{dyn})})|\Phi_{\alpha_{20}}\rangle. \tag{A3}$$

The solution of the linear-response equation thus obtained provides the dynamical response generator $\hat{Q}_\alpha^{(\mathrm{dyn})}$. Note that the whole energy functional is involved in the response. This is called self-consistent, or ATDHF, cranking, see, e.g., [33,49]. The inverse collective mass for quadrupole motion is then obtained in a straightforward manner as

$$B = \frac{1}{2}\left.\frac{\partial^2 E_{\mathrm{SHF}}(|\Phi_{\alpha_{20}p_\alpha}\rangle)}{\partial {p_\alpha}^2}\right|_{p_\alpha=0}$$

$$\equiv \frac{1}{2}\langle\Phi_{\alpha_{20}}|[\hat{Q}_\alpha^{(\mathrm{dyn})},[\hat{H},\hat{Q}_\alpha^{(\mathrm{dyn})}]]|\Phi_{\alpha_{20}}\rangle. \tag{A4}$$

The second form with the double commutator is not strictly applicable in connection with energy functionals (where the full $\hat{H}$ is not given). It serves here only as a notational abbreviation to establish contact with standard formulas for cranking masses.

The same procedure is applied to the dynamical response to rotations. The collective momentum is already known here as it is the angular momentum, e.g., $\hat{J}_x$. Solving the equations for the corresponding dynamical response yields the momentum of inertia as

$$\frac{1}{2\Theta_{xx}} = \frac{1}{2}\left.\frac{\partial^2 E_{\mathrm{SHF}}(|\Phi_{\alpha_{20}\omega}\rangle)}{\partial\omega^2}\right|_{\omega=0}$$

$$\equiv \frac{1}{2}\langle\Phi_{\alpha_{20}}|[\hat{Q}_J^{(\mathrm{dyn})},[\hat{H},\hat{Q}_J^{(\mathrm{dyn})}]]|\Phi_{\alpha_{20}}\rangle, \tag{A5}$$

and similarly for y and z. The operator $\hat{Q}_J^{(\mathrm{dyn})}$ carries the dynamical response in the same manner as $\hat{Q}_\alpha^{(\mathrm{dyn})}$ does that for the quadrupole motion. In practice, we are considering only axially symmetric shapes α_{20}. For them, we obtain

$$\Theta_{xx} = \Theta_{yy} = \Theta,\ \Theta_{zz} = 0.$$

For the case rotation, we simplify the response problem by computing the response with the stationary mean field $\hat{h}$ only (Inglis cranking). The approximation works very well for the considered cases. The critical region of small deformations [50] does not contribute due to the topological switching (A7).

For the full five-dimensional quantum corrections (see the next subsection subsection A 3), we also need to compute the inverse collective mass B_γ and width λ_γ for vibrations in the γ direction. We do that for the vicinity of axial shapes by means of linear response. And we employ here the Inglis approximation using only the mean-field Hamiltonian $\hat{h}$ in the response equations. All together, we have then the necessary ingredients concerning masses: the inverse masses B, $B_\gamma (=B)$, and the momentum of inertia $\Theta(\alpha_{20})$.

3. Quantum corrections

The GCM ansatz for the collectively correlated state is written as a coherent superposition over the path. However, the states of the path correspond to wave packets in quadrupole space rather than to eigenstates of α_{20} (and similarly for the dynamical extensions in p_α and ω_{crank}). Thus they contain spurious contributions from collective motion which contribute to any expectation value. The strongest effects are found in the energy expectation values which constitute the raw collective potential (A2). These spurious contributions need to be subtracted. That is what one calls the quantum corrections or zero-point energies (ZPE) [12].

The correction for spurious center-of-mass motion is already part of the standard SHF scheme. The most important for the collective dynamics is the vibrational-rotational correction. These need to be considered as one entity because vibrations and rotations are closely connected pieces of the nuclear quadrupole topology. The recipe for purely axial vibration and rotation was given in [12,37]. A recent model calculation has confirmed that ansatz and proven that the correction provides also a very good approximation to angular-momentum projection, again for heavy nuclei. Here we want to account for the whole five-dimensional quadrupole dynamics (see Appendix A 5). Thus we are using the properly generalized rotational-vibrational correction

$$E_{\mathrm{quad}}^{(\mathrm{ZPE})} = \frac{\lambda_\beta}{4\mathcal{M}_\beta} + \frac{\partial_\beta^2\mathcal{V}}{4\lambda_\beta}, \tag{A6a}$$

$$\lambda_\beta = 2\langle\Phi_{\alpha_{20}}|\hat{P}_\alpha^2|\Phi_{\alpha_{20}}\rangle,$$

$$\hat{P}_\beta|\Phi_{\alpha_{20}}\rangle = i\partial_\beta|\Phi_{\alpha_{20}}\rangle,$$

$$E_{\mathrm{triax}}^{(\mathrm{ZPE})} = \frac{\lambda_\gamma}{4\mathcal{M}_\gamma} + \frac{\partial_\gamma^2\mathcal{V}}{4\lambda_\gamma} \approx \frac{\lambda_\gamma}{4\mathcal{M}_\gamma}, \tag{A6b}$$

$$E_{\mathrm{rot}}^{(\mathrm{ZPE})} = \frac{\lambda_{\mathrm{rot}}}{4\Theta}, \tag{A6c}$$

$$\lambda_{\mathrm{rot}} = 2\langle\Phi_{\alpha_{20}}|\hat{J}_{x,y}^2|\Phi_{\alpha_{20}}\rangle, \tag{A6d}$$

where $\hat{J}_{x,y}$ is the angular momentum about the x or y axis. The widths are the same for x and y because we evaluate

everything at axial symmetry, i.e., at the point $\gamma=0$. The total ZPE is decomposed as

$$E_{\rm tot}^{\rm (ZPE)}(\alpha_{20}) = \left[5 - 4g\left(\frac{\lambda_{\rm rot}}{4}\right)\right]E_{\rm quad}^{\rm (ZPE)} + 2g\left(\frac{\lambda_{\rm rot}}{4}\right)E_{\rm rot}^{\rm (ZPE)} + 2g\left(\frac{\lambda_{\rm rot}}{4}\right)E_{\rm triax}^{\rm (ZPE)}, \tag{A7a}$$

$$g(a) = \frac{\int_0^1 dx a(x^2-1)e^{a(x^2-1)}}{\int_0^1 dx e^{a(x^2-1)}}. \tag{A7b}$$

There is also a correction from spurious particle number fluctuations. This is already taken into account in an approximate manner by the Lipkin-Nogami scheme added on top of the BCS pairing.

All together, the quantum-corrected collective potential reads

$$V(\alpha_{20}) = \mathcal{V}(\alpha_{20}) - E_{\rm tot}^{\rm (ZPE)}(\alpha_{20}). \tag{A8}$$

This is the quantity entering the collective Hamiltonian. The masses are associated with the collective kinetic energies which are already of second order in the collective momenta. The quantum corrections on masses would correspond to terms of fourth order and are neglected.

4. Retuning the particle number

All states along the collective path are tuned to have the same average proton and neutron number. The energies are corrected by approximate particle-number projection at the level of the LN scheme. But the BCS states from which the collective path is composed still carry these particle-number fluctuations. As a consequence, the coherent superposition of the states along the path may change the average particle number again. One needs to readjust the correct average at the level of the collective dynamics [51]. To that end, one builds the collective picture of the particle number operator $\hat{N}-N$ in precisely the same manner as was done for the Hamiltonian. One obtains a particle-number potential, particle-number masses for quadrupole as well as triaxial motion, and particle-number contributions to the inertia. The expressions are the same as above with $\hat{H}$ replaced by $\hat{N}$. The collective image of $\hat{N}$ is added as a constraint in the collective Schrödinger equation.

5. The collective Schrödinger equation

Axially symmetric quadrupole deformations are labeled by α_{20}. The full space of quadrupole deformations is explored when considering all α_{2m} with $m\in\{-2,-1,0,1,2\}$. This is convenient for spherical vibrator nuclei as it implies automatically the correct number of vibrational degrees of freedom. It is, however, not well suited for deformed nuclei because rotations look rather involved in that frame. It is customary to transform by appropriate rotation into an intrinsic frame where $a_{2\pm1}=0$ and $a_{22}=a_{2-2}$. This defines three Euler angles ϑ as rotational coordinates. The remaining two relevant deformation coordinates a_{20} and a_{22} are expressed in terms of total deformation β and triaxiality γ as $a_{20}=\beta\cos(\gamma)$ and $a_{22}=\beta\sin(\gamma)/\sqrt{2}$ [20,52]. Each triaxiality γ which is an integer multiple of 60° corresponds to an axially symmetric shape. The cases $\gamma=0°$, 120°, and 240° correspond to prolate axial deformations while $\gamma=60°$, 180°, and 300° are oblate. Relevant information is contained in one 60° sector of the plane, e.g., in the segment $\gamma\in[0°,60°]$. The other segments can be reconstructed by axis exchange of principal axes. This symmetry under axis transformation has important consequences for the representation of wave functions and potentials in the collective Schrödinger equation: One has to obey mirror symmetry under $\gamma\rightarrow-\gamma$ and axis-rotation symmetry under $\gamma\rightarrow\gamma+120°$. The five-dimensional volume element d^5a reads in the β-γ frame $d^5a=\beta^4|\sin(3\gamma)|d\beta d\gamma d^3\theta$, where the θ are the three Euler angles for the transformation from the laboratory frame into the intrinsic frame. In the following, we will use the notation $d^5\alpha$ as shorthand for the lengthy right-hand side.

The collective Hamiltonian has the form of a Bohr-Hamiltonian [1,3] generalized to β-γ-dependent masses (A9a) [16,18,19],

$$\hat{H}^{\rm (coll)} = -\frac{1}{\beta^4}\partial_\beta B(\beta,\gamma)\beta^4\partial_\beta - \frac{1}{\beta^2\sin 3\gamma}\partial_\gamma B_\gamma(\beta,\gamma)\sin 3\gamma\partial_\gamma + \sum_{k=1}^{3}\frac{\hat{L}_k'^2}{2\Theta_k(\beta,\gamma)} + V(\beta,\gamma), \tag{A9a}$$

$$X(\beta,\gamma) = \frac{X(\beta)+X(-\beta)}{2} + \frac{X(\beta)-X(-\beta)}{2}\cos(3\gamma), \quad X\in\{B,V\}, \tag{A9b}$$

$$\frac{1}{\Theta_k(\beta,\gamma)} = \frac{3}{4\sin^2\left(\gamma-\frac{2\pi}{3}k\right)}\left[\frac{1}{2}\left(\frac{1}{\Theta(\beta)}+\frac{1}{\Theta(-\beta)}\right) + \left(\frac{1}{\Theta(\beta)} - \frac{1}{\Theta(-\beta)}\right)\cos\left(\gamma-\frac{2\pi}{3}k\right)\right], \quad k\in\{1,2,3\} \tag{A9c}$$

$$\langle q|LM\rangle = \Psi^{LM}(\beta,\gamma,\vartheta_i) = \sum_\nu \psi_\nu^L(\beta)\chi_\nu^{LM}(\gamma,\vartheta_i), \ \nu=0,1,\ldots, \tag{A10a}$$

$$\{\chi_\nu^{00}(\gamma,\vartheta_i),\nu=0,1,\ldots\} = \mathcal{O}\{\cos(3\nu\gamma)D_{00}^{(0)}\} = \left\{\sqrt{\frac{2\nu+1}{32\pi^2}}P_\nu[\cos(3\gamma)]\right\}, \tag{A10b}$$

$$\{\chi_\nu^{2M}(\gamma,\vartheta_i),\nu=0,1,\ldots\} = \mathcal{O}\left\{\cos(\lambda\gamma)D^{(2)}_{M0} - (-1)^{\lambda\%3}\sin(\lambda\gamma)\frac{D^{(2)}_{M,-2}+D^{(2)}_{M,2}}{\sqrt{2}}\right\}, \tag{A10c}$$

$$\lambda = 3\left[\frac{\nu}{2}\right] + \nu\%2 + 1,$$

where $\mathcal{O}$ means orthonormalization of the set, $[\cdots]$ the integer part of a fraction, and $a\%b$ the modulo of a with respect to b. The operator $\hat{L}'_k$ denotes the angular momentum in the intrinsic frame. The deformed SHF calculations provide input along axially symmetric deformations $a_{20}\gtrless 0$. The collective dynamics needs to be performed properly in all five quadrupole degrees of freedom. No strong peaks or wells in the γ direction are to be expected for the nearly spherical or weakly deformed soft vibrator nuclei which we will consider here. It is thus an acceptable approach to interpolate the axial microscopic results into the full β-γ plane. While potential, inverse masses, and particle-number masses could be interpolated in a straightforward manner by Eq. (A9b), the moment of inertia has three components. Respecting the collective symmetries, we reconstruct them from the axial information as Eq. (A9c). The deduction from axial information implies that we neglect the β-γ coupling in the kinetic energy, i.e., $B_{\beta\gamma}=0$. The collective particle-number operator $\hat{H}^{(\mathrm{coll})}$ is composed in the same form with the corresponding particle-number masses, potentials, and moments of inertia inserted.

The collective Schrödinger equations read now

$$(\hat{H}^{(\mathrm{coll})} - \epsilon_{\mathrm{F}}^{\mathrm{coll}}\hat{N}^{(\mathrm{coll})})\Psi = E\Psi, \tag{A11}$$

where the correction of the Fermi energy $\epsilon_{\mathrm{F}}^{\mathrm{coll}}$ is to be adjusted such that $\int d^5a\Psi^+\hat{N}^{(\mathrm{coll})}\Psi = N$.

The dynamics is formulated in the whole β-γ plane but all necessary information is contained already in a segment of 60°, as discussed in Appendix A 5. In order to meet the inherent symmetry conditions [1], the wave functions of a 0^+ and a 2^+ state are expanded in a symmetrized base (A10) where the base mode $\nu=0$ determines the overall β dependence and the higher ν shape the profile in the γ direction. The Hamiltonian is very soft in γ such that few ν terms suffice for convergence (two or three, never more than five). The $D^{(L)}_{M,K}(\vartheta)$ are the well known Wigner D functions describing the rotation matrices for a state with angular momentum L [53]. It is noteworthy that the structure of the rotational energy is that for the most general case where the considered nuclei have no special symmetry. For that reason the 2^+ state must be a sum over all possible z projections of the angular momentum which are $K=0,\pm 2$ in the intrinsic frame.

The remaining collective equation for the components $\psi^L_\nu(\beta)$ is solved numerically with standard methods. The wave functions and fields are represented on an equidistant grid in β. Gradient iteration is used to find the few lowest eigenvalues and states.

6. Computation of observables

The solution of the collective Schrödinger equation, as outlined in the previous section, provides the energies directly. Expectation values and transition moments of other observables $\hat{O}$ need yet to be computed. The steps are, in principle, the same as done before for the energy (= Hamiltonian $\hat{H}$, respectively) and for the particle number $\hat{N}$. One has first to determine the collective image of the given observable $\hat{O}\rightarrow O_{\mathrm{coll}}$ and computes then the expectation value of that image with the collective wave functions [12]. Actually, we do that for the computation of the transition probabilities $0^+\rightarrow 2^+$, the proton $B(E2)$ values. The observable here is $\hat{O}\equiv\hat{Q}_{20,\mathrm{prot}}$. In the case of the isotope shifts, the observable is the collective mapping of the radius. At present, we approximate the collective image by the raw expectation value only and neglect the kinetic corrections.

[1] J. Eisenberg and W. Greiner, *Nuclear Models* (North-Holland Publishing Company, Amsterdam, 1970), Vol. 1.
[2] Å. Bohr and B. R. Mottelson, *Nuclear Structure. Nuclear Deformations* (W. A. Benjamin Inc., London, 1975), Vol. 2.
[3] A. Bohr, Mat. Fys. Medd. K. Dan. Vidensk. Selsk. **26**, No. 14 (1952).
[4] G. Gneuss and W. Greiner, Nucl. Phys. **A171**, 449 (1971).
[5] F. Iachello and A. Arima, *The Interacting Boson Model* (Cambridge University Press, Cambridge, England, 1987).
[6] M. Goeppert-Mayer, Phys. Rev. **74**, 235 (1948).
[7] O. Haxel, J. Jensen, and H. Suess, Naturwissenschaften **36**, 155 (1949).
[8] G. E. Brown, *Unified Theory of Nuclear Models and Forces*, 3rd ed. (North-Holland, Amsterdam, 1971).
[9] D. J. Rowe, *Nuclear Collective Motion* (Methuen, London, 1970).
[10] D. L. Hill and J. A. Wheeler, Phys. Rev. **89**, 1102 (1953).
[11] J. J. Griffin and J. A. Wheeler, Phys. Rev. **108**, 311 (1957).
[12] P.-G. Reinhard and K. Goeke, Rep. Prog. Phys. **50**, 1 (1987).
[13] P. Bonche, J. Dobaczewski, H. Flocard, P. H. Heenen, and J. Meyer, Nucl. Phys. **A510**, 466 (1990).
[14] A. Valor, P.-H. Heenen, and P. Bonche, Nucl. Phys. **A671**, 145 (2000).
[15] R. Rodriguez-Guzmán, J. L. Egido, and L. M. Robledo, Phys. Rev. C **65**, 024304 (2002).
[16] L. Próchniak, K. Zaj, K. Pomorski, S. G. Rohoziński, and J. Srebrny, Nucl. Phys. **A648**, 181 (1999).
[17] M. Girod and P.-G. Reinhard, Nucl. Phys. **A384**, 179 (1982).
[18] J. Libert, M. Girod, and J.-P. Delaroche, Phys. Rev. C **60**, 054301 (1999).
[19] L. Prochniak, P. Quentin, D. Samsoen, and J. Libert, Nucl. Phys. **A730**, 59 (2004).

[20] P. Ring and P. Schuck, *The Nuclear Many-Body Problem* (Springer-Verlag, New York, 1980).
[21] J. Terasaki, J. Engel, M. Bender, J. Dobaczewski, W. Nazarewicz, and M. Stoitsov, nucl-th/0407111.
[22] K. Goeke and P.-G. Reinhard, Ann. Phys. (N.Y.) **124**, 249 (1980).
[23] M. Bender, P.-H. Heenen, and P.-G. Reinhard, Rev. Mod. Phys. **75**, 121 (2003).
[24] P.-G. Reinhard, M. Bender, and J. A. Maruhn, Comments Mod. Phys. A **2**, 177 (2002).
[25] J. Bartel, P. Quentin, M. Brack, C. Guet, and H.-B. Håkansson, Nucl. Phys. **A386**, 79 (1982).
[26] P.-G. Reinhard and H. Flocard, Nucl. Phys. **A584**, 467 (1995).
[27] E. Chabanat, Ph.D. thesis, Université Claude Bernard Lyon-1 (1995).
[28] E. Chabanat, P. Bonche, P. Haensel, J. Meyer, and R. Schaeffer, Nucl. Phys. **A627**, 710 (1997).
[29] P.-G. Reinhard, D. J. Dean, W. Nazarewicz, J. Dobaczewski, J. A. Maruhn, and M. R. Strayer, Phys. Rev. C **60**, 014316 (1999).
[30] J. Terasaki, P.-H. Heenen, P. Bonche, J. Dobaczewski, and H. Flocard, Nucl. Phys. **A593**, 1 (1995).
[31] M. Bender, K. Rutz, P.-G. Reinhard, and J. A. Maruhn, Eur. Phys. J. A **8**, 59 (2000).
[32] M. Baranger and M. Véneroni, Ann. Phys. (N.Y.) **114**, 123 (1978).
[33] K. Goeke and P.-G. Reinhard, Ann. Phys. (N.Y.) **112**, 328 (1978).
[34] A. Klein, N. R. Walet, and G. DoDang, Ann. Phys. (N.Y.) **208**, 90 (1990).
[35] P. Bonche, J. Dobaczewski, H. Flocard, and P.-H. Heenen, Nucl. Phys. **A530**, 149 (1991).
[36] K. Hagino, P.-G. Reinhard, and G. F. Bertsch, Phys. Rev. C **65**, 064320 (2002).
[37] P.-G. Reinhard, Z. Phys. A **285**, 93 (1978).
[38] http://www.nndc.bnl.gov/nndc/nudat/levform.html, Accessed: May 2003.
[39] P. Fleischer, P. Klüpfel, T. Cornelius, T. Bürvenich, S. Schramm, J. Maruhn, and P.-G. Reinhard (unpublished).
[40] I. Hamamoto and H. Sagawa, Phys. Rev. C **54**, 2369 (1996).
[41] J. Terasaki, J. Engel, W. Nazarewicz, and M. Stoitsov, Phys. Rev. C **66**, 054313 (2002).
[42] J. Dobaczewski, P. Magierski, W. Nazarewicz, W. Satula, and Z. Szymanski, Phys. Rev. C **63**, 024308 (2001).
[43] J. L. Wood, K. Heyde, W. Nazarewicz, M. Huyse, and P. van Duppen, Phys. Rep. **215**, 101 (1992).
[44] J. Eberz, U. Dinger, G. Huber, H. Lochmann, R. Menges, G. Ulm, R. Kirchner, O. Klepper, T. U. Kühl, and D. Marx, Z. Phys. A **326**, 121 (1987).
[45] P.-G. Reinhard, W. Nazarewicz, M. Bender, and J. A. Maruhn, Phys. Rev. C **53**, 2776 (1996).
[46] K. Rutz, J. A. Maruhn, P.-G. Reinhard, and W. Greiner, Nucl. Phys. **A590**, 680 (1995).
[47] P.-G. Reinhard and R. Y. Cusson, Nucl. Phys. **A378**, 418 (1982).
[48] R. Y. Cusson, P.-G. Reinhard, M. R. Strayer, J. A. Maruhn, and W. Greiner, Z. Phys. A **320**, 475 (1985).
[49] J. Dobaczewski and J. Skalski, Nucl. Phys. **A369**, 123 (1981).
[50] P.-G. Reinhard, F. Grümmer, and K. Goeke, Z. Phys. A **317**, 339 (1984).
[51] A. Valor, J. L. Egido, and L. M. Robledo, Nucl. Phys. **A671**, 189 (2000).
[52] W. Greiner and J. A. Maruhn, *Kernmodelle*, Vol. 11 of *Theoretische Physik* (Verl. Harri Deutsch, Thun, Frankfurt am Main, 1995).
[53] A. R. Edmonds, *Angular Momentum in Quantum Mechanics* (Princeton University Press, Princeton, NJ, 1964).